

Proximity-tuned Magnetic and Transport Anomalies in All-epitaxial $\text{Fe}_{5-x}\text{GeTe}_2/\text{WSe}_2$ Van der Waals Heterostructures

Hua Lv*, Tausiqir Shinwari, Kacho Imtiyaz Ali Khan, Jens Herfort, Chen Chen, Joan M. Redwing, Mehak Loyal, Gerhard Jakob, Mathias Kläui, Achim Trampert, Bernat Mundet, Belén Ballesteros, Manfred Ramsteiner, Roman Engel-Herbert, Michael Hanke, João Marcelo J. Lopes*

Dr. H. Lv, Dr. T. Shinwari, Dr. K. I. A. Khan, Dr. J. Herfort, Dr. A. Trampert, Dr. M. Ramsteiner, Prof. Dr. R. Engel-Herbert, PD Dr. M. Hanke, Dr. J. M. J. Lopes

Paul-Drude-Institut für Festkörperelektronik, Leibniz-Institut im Forschungsverbund Berlin e. V., Hausvogteiplatz 5–7, 10117 Berlin, Germany

Email Address: hua.lv@pdi-berlin.de, lopes@pdi-berlin.de

Dr. C. Chen, Prof. Dr. J. M. Redwing

2D Crystal Consortium Materials Innovation Platform, Materials Research Institute, The Pennsylvania State University, University Park, PA 16802, United States

M.S. M. Loyal, Prof. Dr. G. Jakob, Prof. Dr. M. Kläui

Institute of Physics, Johannes Gutenberg University Mainz, Staudingerweg 7, 55128 Mainz, Germany

Dr. B. Mundet, Dr. B. Ballesteros

Catalan Institute of Nanoscience and Nanotechnology (ICN2), CSIC and The Barcelona Institute of Science and Technology (BIST), Campus UAB, Bellaterra, 08193 Barcelona, Spain

Keywords: *van der Waals heterostructures, proximity effect, unconventional Hall effect, exchange bias effect, perpendicular magnetic anisotropy, molecular beam epitaxy*

Van der Waals (vdW) heterostructures combining two-dimensional (2D) ferromagnets and semiconducting transition-metal dichalcogenides (TMDCs) offer highly promising opportunities for tailoring 2D magnetism through interfacial proximity effects, enabling unique physical phenomena inaccessible in 3D systems and achieving functionalities beyond conventional spintronics. However, current fabrication of vdW heterostructures still relies heavily on the manual stacking of exfoliated 2D flakes, leading to critical challenges in scalability, interfacial quality, thickness control and device integration. This work reports on the realization of all-epitaxial, high-quality $\text{Fe}_{5-x}\text{GeTe}_2$ (FGT)/ WSe_2 heterostructures exhibiting perpendicular magnetic anisotropy (PMA) and room-temperature ferromagnetism. The FGT/ WSe_2 system demonstrates temperature-driven magnetic transitions, higher-order PMA contributions and large anisotropic magnetoresistance, highlighting sublattice-specific contributions to magnetic and transport properties. Notably, the FGT/ WSe_2 heterostructures display unconventional physical phenomena, including thickness- and temperature-dependent sign reversal of exchange bias, a reversed thickness trend in the unconventional Hall effect, and a non-monotonic PMA-thickness dependence. These anomalies indicate pronounced interfacial contributions arising from proximity effects enhanced by epitaxial interface quality. Collectively, this study provides deep insights into the magnetic and transport properties of FGT/ WSe_2 vdW heterostructures, establishing a scalable platform for exploring emergent 2D physics and advancing next-generation 2D spintronic technologies.

1 Introduction

The emergence of two-dimensional (2D) ferromagnets is driving a paradigm shift in magnetism research.^[1–5] While 3D magnetic materials have been extensively explored over the past century and underpin modern information technology, atomically thin 2D magnets are now at the forefront, promising to reveal novel magnetic phenomena and enable device concepts previously unattainable.^[6–11] Furthermore, magnetic heterostructures integrating different materials can provide great opportunities to engineer magnetic and transport properties, induce novel interfacial phenomena and achieve functionalities impossible in single materials.^[7,8,12] However, conventional 3D heterostructures require strict lattice matching and often suffer from interlayer mixing and magnetic dead layers, which significantly degrade the interface quality and suppress interface-driven physics, representing a long-standing issue.^[13–16] In contrast, van der Waals (vdW) heterostructures can be constructed from lattice-mismatched materials, which enables atomically sharp and strain-free interfaces,^[7,8,12,17,18] thereby significantly enhancing coupling between adjacent layers.^[6,7,19–21] In

particular, 2D magnets and vdW heterostructures provide a promising platform for exploring phenomena that are absent or strongly suppressed in 3D systems, including: (i) proximity effects, offering an efficient but largely underexplored route to tune magnetic and transport properties;^[7,19] (ii) 2D exchange bias, an essential step for realizing 2D spintronic devices;^[20,22–26] and (iii) unconventional spin transport and topological spin textures, which probe Berry curvature and hold strong promise for high-density racetrack memories.^[27–32] Investigating them not only deepens the fundamental understanding but also opens avenues for novel functionalities, effectively bridging conventional 3D spintronics with its 2D counterpart. However, systematic studies are still in their infancy, with many emerging 2D phenomena and underlying mechanisms yet to be explored.

Among various 2D magnets, Fe–Ge(Ga)–Te compounds stand out as prototypical material systems by combining high Curie temperature (T_C) and intrinsic metallic behavior, both of which are essential for spintronic applications.^[3,4,18,33–36] Within this family, metallic Fe_5GeTe_2 (FGT) exhibits a T_C near room temperature, positioning it as one of the leading material candidates.^[4,18,33] Beyond high T_C , perpendicular magnetic anisotropy (PMA) is critical for achieving low-power magnetization operation and high thermal stability, playing a key role in non-volatile magnetic memory technologies.^[37,38] However, conventional 3D PMA materials, such as CoFeB/MgO and $[\text{Co}/\text{Pt}]_n$ -like multilayers, require sub-nanometer thickness precision to maintain strong PMA, leading to significant challenges for scalable fabrication.^[38–40] Identifying PMA materials without such thickness constraints is crucial for modern spintronics but remains an unmet goal.^[38] Previous studies of FGT in exfoliated flakes typically exhibit in-plane magnetic anisotropy (IMA),^[41–43] thereby strongly limiting their spintronic applications. Furthermore, to build FGT-based heterostructures, 2D semiconducting transition-metal dichalcogenides (TMDCs) are particularly attractive partners due to their strong spin–orbit coupling (SOC) and unique optical response.^[21] Fundamentally, FGT/TMDC heterostructures could offer a platform to exploit proximity-induced phenomena without introducing additional magnetic and transport signals on FGT, including PMA modulation and skyrmion formation.^[44] From an application perspective, such heterostructures promise large spin-orbit torque (SOT) effects^[45] and optical spin injection, providing an ideal platform for combining spin-orbitronic and opto-spintronic functionalities.^[21] However, most demonstrations of 2D magnets and related vdW heterostructures have primarily relied on exfoliated flakes assembled manually, which are typically limited to micrometer dimensions and thus incompatible with scalable device fabrication.^[10,11,46] For both fundamental studies and practical applications, achieving large-scale epitaxial growth of 2D magnets and vdW heterostructures is therefore essential.^[6,10,11] Indeed, following the investigation of various 2D materials in bulk crystal form, achieving large-scale epitaxial synthesis is highly demanded for future applications.^[11,18,47–49] However, despite recent progress in scalable fabrication of vdW heterostructures,^[18,36,50] all-epitaxial growth of 2D magnet/TMDC heterostructures with near-room-temperature magnetism have not yet been realized, representing a critical bottleneck for advancing 2D spintronic applications.^[21]

In this work, we report the realization of large-area, all-epitaxial FGT/TMDC vdW heterostructures, here using WSe_2 as the TMDC, which exhibit atomically sharp interfaces and room-temperature ferromagnetism with PMA. The observed temperature-driven magnetic transitions, higher-order PMA and pronounced anisotropic magnetoresistance (AMR) highlight sublattice-specific contributions to the magnetic and transport properties. Strikingly, the FGT/ WSe_2 heterostructures reveal a series of unconventional phenomena associated with their 2D nature, including a temperature- and thickness-dependent sign reversal of exchange bias, a non-monotonic PMA–thickness dependence, and a reversed thickness trend in the unconventional Hall effect (UHE). These phenomena indicate pronounced interfacial contributions, suggesting a strong proximity effect enabled by the high FGT/ WSe_2 interface quality. This work not only provides deeper insights into the magnetic and transport properties of FGT/ WSe_2 vdW heterostructures but also establishes an excellent platform for exploring emergent 2D physics and developing next-generation spintronic technologies.

2 Results and Discussion

2.1 Structural properties

Molecular beam epitaxy (MBE) was employed to grow FGT films with thicknesses (t_{FGT}) of 6, 12 and 17 nm directly on single-crystalline, continuous monolayer–bilayer thick WSe₂ synthesized by chemical vapor deposition (CVD) on Al₂O₃(0001).^[47] The FGT growth process was continuously monitored via in-situ reflection-high-energy-electron-diffraction (RHEED, Figure S1, Supporting Information), which confirmed the epitaxial growth of FGT films having a smooth 2D surface. The FGT films were capped *in-situ* with a Te layer (5 nm) deposited at room temperature. Fe_{5-x}GeTe₂ is usually a non-stoichiometric system,^[51,52] with $x \approx 0.2$ in our case.^[18]

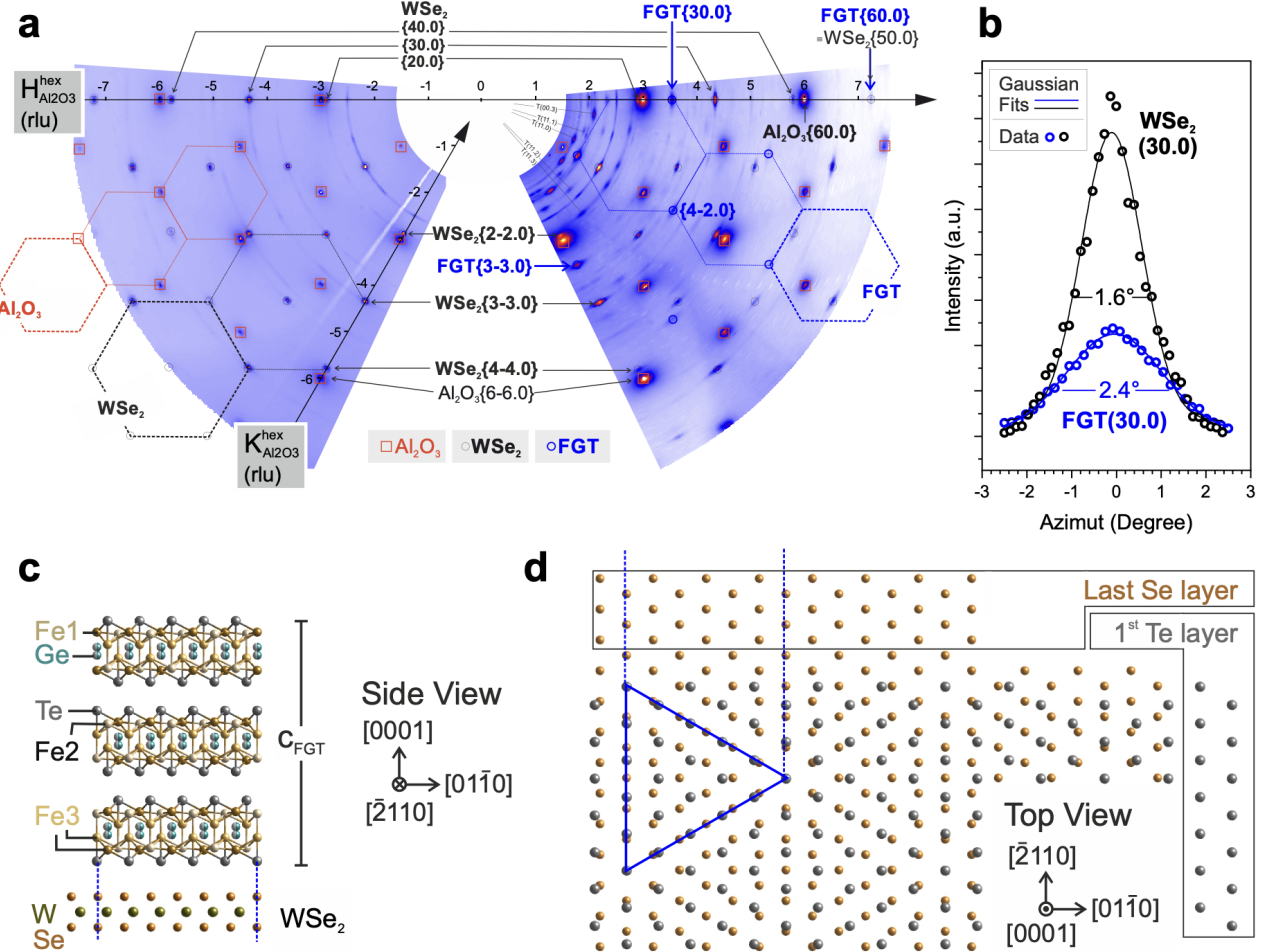


Figure 1: a) In-plane reciprocal space maps: (left) bare WSe₂/Al₂O₃(0001) and (right) 17 nm FGT/WSe₂/Al₂O₃(0001). Due to trigonal symmetry, the H and K axes form an angle of 60°. b) Angular scans intersecting the WSe₂ and FGT(30.0) reflections in the space map shown in the right panel of a). c,d) Schematics of the structural configuration of the synthesized FGT/WSe₂ stack according to the epitaxial alignment determined by GID: c) side-view, d) top-view. For simplicity, d) shows only the last, topmost Se layer in WSe₂ and the first Te layer in FGT. The blue triangle indicates the coincidence-site lattice matching between WSe₂ and FGT.

The structural properties of the samples were investigated in detail by synchrotron-based grazing incidence diffraction (GID), a tool of choice for probing in-plane properties such as strain and crystallographic orientation of 2D layers.^[53] Due to the evanescent X-ray wave field in the crystal, GID becomes an extremely surface-sensitive approach. **Figure 1a** shows two reciprocal space maps probed by GID. They cover a relatively large area, i.e., azimuthally a range of $\pm 35^\circ$ and in radial direction scattering vectors far beyond the in-plane Al₂O₃ (60.0) reflection. The reciprocal space map shown left was obtained for a pristine WSe₂/Al₂O₃(0001) samples, while the right one

was taken for a 17 nm FGT/WSe₂/Al₂O₃(0001) sample. The former serves as a reference for the sample with an additional FGT layer on top (right). To disentangle the different scattering contributions from sapphire, WSe₂ and FGT, we have marked the respective positions and connected some of them with dashed lines. This gives a clear view of the crystallographic orientation, with the [10.0] substrate direction coinciding exactly with that of FGT and WSe₂. Despite the weak vdW bonding, a well-defined in-plane epitaxial relation between the two layers is preserved. This epitaxial alignment is also evidenced by azimuthal scans, as depicted in Figure 1b for the FGT(30.0) and WSe₂(30.0) in-plane reflections. Both angular widths, i.e. the full width at half maximum values (1.6° for the WSe₂ layer and 2.4° for FGT) are rather small considering what is usually measured for epitaxially grown vdW materials.^[18,54] Note that, since the FGT/WSe₂ stack was covered by a Te capping layer, we could also probe the signature of metallic tellurium by a set of reflections rather close to the center.

Taking the radial distance for a set of reflections for FGT and WSe₂, we could precisely determine the in-plane lattice parameters: for FGT, a value $a_{\text{FGT}} = 4.032(10)$ Å was found, while for WSe₂ the values $a_{\text{WSe}_2} = 3.299(10)$ Å and $a_{\text{WSe}_2} = 3.273(10)$ Å were obtained for pristine and FGT-overgrown films, respectively. These values are in good agreement with what has been reported for bulk crystals and thin films grown on different substrates.^[18,33,54-57] The smaller in-plane lattice constant observed in WSe₂ overgrown by FGT may be related to defect formation in WSe₂ during the MBE process. In particular, heating the sample in the ultra-high vacuum (UHV) environment of MBE may cause some Se to desorb, resulting in vacancy formation and local lattice contractions.^[58] This, in turn, may lead to a small reduction in the average lattice constant, which GID can detect.^[59] Nevertheless, the clear observation of several GID reflections associated with WSe₂ serves as concrete evidence that the TMDC layer preserves its overall structure after FGT growth. This is further supported by Raman spectroscopy measurements (Figure S2, Supporting Information). Finally, it is important to point out that GID reveals a coincidence-site lattice matching between FGT and WSe₂, with a resulting ratio $5a_{\text{FGT}} \approx 6a_{\text{WSe}_2}$. This likely contributes to the strong in-plane registry between both materials, as previously reported for other epitaxial vdW systems.^[60] The epitaxial orientation and coincidence-site lattice matching between the FGT and WSe₂ layers are depicted schematically in Figure 1c,d. Furthermore, GID reveals very similar structural properties for FGT films of different thicknesses (Figure S3, Supporting Information).

Scanning transmission electron microscopy (STEM) was also employed to investigate the structural properties of the layers. **Figure 2a** shows a high-angle annular dark-field (HAADF)-STEM cross-sectional image of the FGT/WSe₂ heterostructure acquired in a region where the WSe₂ film is monolayer thick. A similar image obtained in a region of bilayer WSe₂ is depicted in Figure S4, Supporting Information. The layered structure of the FGT film is clearly visible, in that single FGT layers are separated by vdW gaps. This is consistent with previous TEM characterization of FGT bulk crystals and thin films.^[18,33,55] By analyzing images obtained from different regions, it was found that the FGT film comprises not only Fe₅GeTe₂ layers (with a monolayer thickness of 1 nm), but also with thicknesses ranging from 1 to 0.8 nm. The latter value, for example, is in very good agreement with the thickness of a Fe₃GeTe₂ single layer.^[61] The average thickness of the FGT single layers obtained from TEM was found to be 0.93 nm. We attribute the stacking disorder in the FGT film — namely, coexistence of layers with slightly different thicknesses and potentially different Fe compositions — to the relatively low substrate temperature employed for the growth of FGT (260°C). Previous studies on MBE growth of FGT films on substrates other than WSe₂ (e.g., Al₂O₃, Bi₂Te₃) have shown that higher growth temperatures and/or post-growth annealing favor stabilization of Fe_{5-x}GeTe₂ phases with a higher Fe concentration, such as Fe₅GeTe₂ (i.e., $x = 0$).^[55,62] In this study, a low growth temperature was intentionally chosen to mitigate the possible intermixing at the FGT/WSe₂ interface. This strategy proved successful, as the electron energy loss spectroscopy (EELS) mappings show a fairly homogeneous distribution of each element with no intermixing between adjacent layers (see Figure 2b). As expected for FGT (see Figure 1c), Fe and Ge are usually positioned at the center of the FGT layers between the outer Te slabs, while W and Se are present where WSe₂ is located. Note that a region with different contrast can be

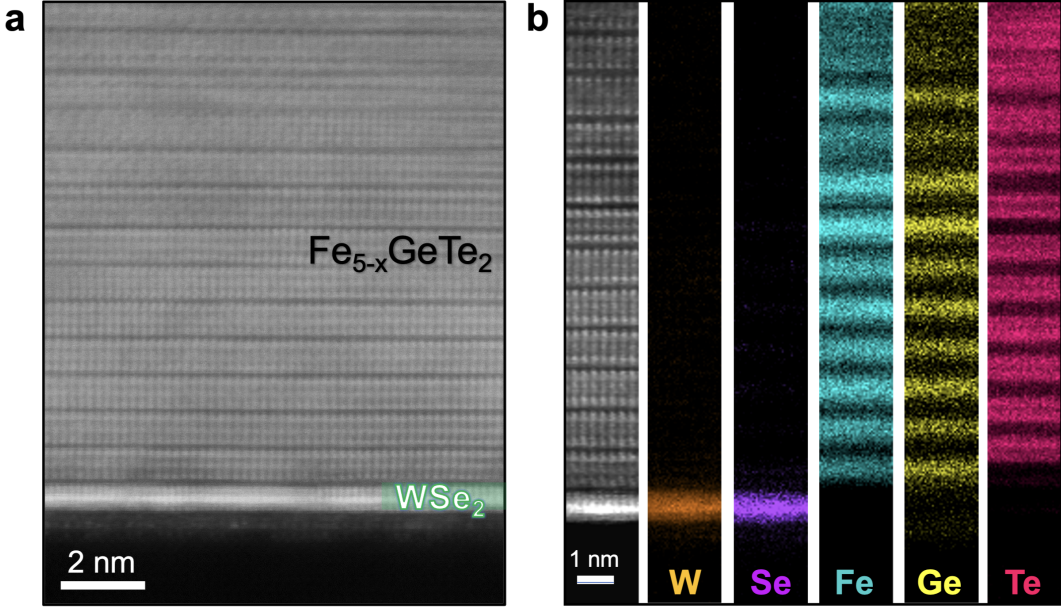


Figure 2: a) STEM cross-section image of a 12 nm thick FGT film grown on $\text{WSe}_2/\text{Al}_2\text{O}_3(0001)$. b) STEM image (left) and the EELS compositional maps for W (orange), S (purple), Fe (blue), Ge (yellow) and Te (red) obtained from the same region.

observed directly below the WSe_2 film at the WSe_2 /sapphire interface (see Figures 2a and S4). This is due to the formation of a Se passivation layer, as discussed in detail previously.^[47]

2.2 Magnetic properties

The magnetic properties of FGT/ WSe_2 vdW heterostructures were investigated using superconducting quantum interference device (SQUID) magnetometry. **Figure 3a** presents the hysteresis loops normalized by the saturation magnetization (M_S) after subtracting a linear background (see raw data in Figure S5, Supporting Information), for a 17 nm thick FGT sample measured at 20 K with a magnetic field (H) applied along the out-of-plane (OP, black) and in-plane (IP, blue) directions. The markedly higher coercive field (H_C) and lower saturation field (H_S) observed in the OP compared to the IP configuration indicate a strong PMA. Notably, the OP hysteresis loop exhibits an unconventional shape with a kink near the zero field (see also Figure S6, Supporting Information). To interpret this feature, an empirical model was developed based on the Boltzmann sigmoid function (Text S1, Supporting Information):

$$\frac{M(H)}{M_S} = 1 - \frac{2}{1 + e^{\frac{H \pm H_C}{(H_S \pm H_C)/4}}} \quad (1)$$

Equation (1) provides a concise description of the hysteresis loop using only the directly measurable parameters of H_C and H_S . This approach offers significant advantages over more complex models, such as the Jiles-Atherton model based on the Langevin function,^[63] particularly for quantitative analyses and simulations. The OP hysteresis loop can be well fitted by Equation (1) (red curves) when incorporating a square-shaped phase (pink curves) and a zero-coercivity contribution (green curve) (see Text S1, Supporting Information). The square-shaped phase is attributed to the strong PMA of FGT and closely matches the anomalous Hall effect (AHE) signal (see the next section). The zero-coercivity contribution, given its absence in the AHE measurement, is unlikely to originate from the metallic FGT phase. It may arise from the formation of oxidized FGT (O-FGT), a possibility that will be further discussed alongside the transport measurements.

Figure 3b illustrates the temperature-dependent magnetization measured during zero-field warming up after setting the initial magnetization with a 1 T field. The inset displays the normalized remanent magnetization (M_R/M_S), with M_R obtained at zero field from the $M - H$ curves (Figure

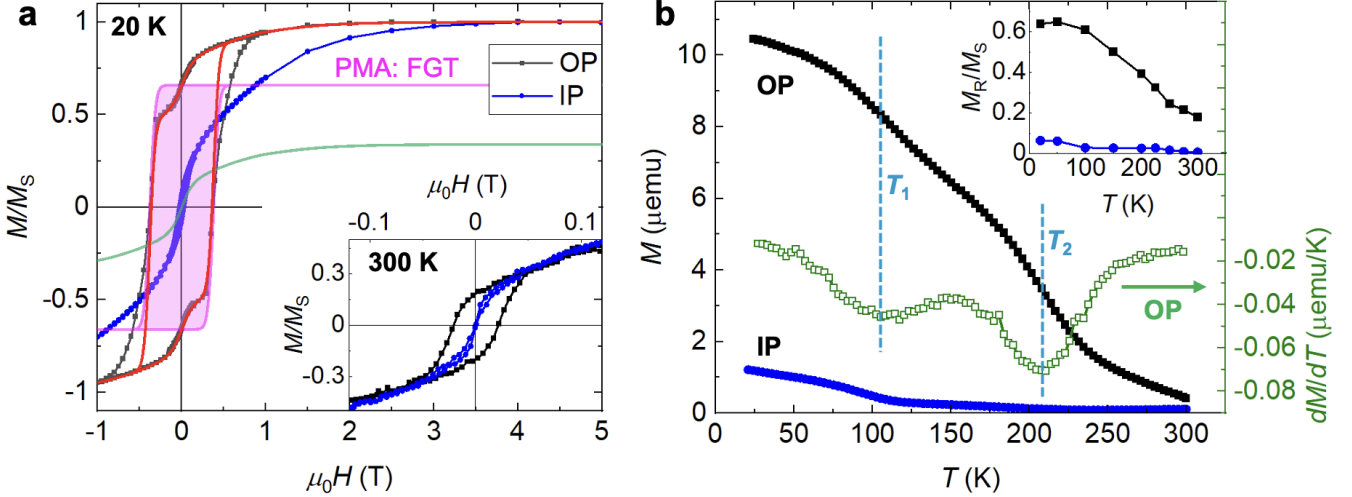


Figure 3: Magnetic characterization of a 17 nm FGT/WSe₂ vdW heterostructure using SQUID magnetometry. a) Normalized magnetization M/M_S as a function of out-of-plane (OP, black) and in-plane (IP, blue) magnetic fields at 20 K. Red curves are fits based on Equation (1), comprising a square-shaped PMA component (pink) and a zero-coercivity contribution (green). Inset: normalized hysteresis loops at 300 K. b) Temperature-dependent magnetization M during zero-field warming. The green curve shows the first derivative dM/dT in the OP configuration. Inset: M_R/M_S extracted from the hysteresis loops at each temperature.

3a). The larger M_R in the OP configuration indicates the persistence of PMA and ferromagnetic ordering up to room temperature. Both the OP $M - T$ curve (black) and its derivative dM/dT (green) exhibit two clear magnetic transitions at temperatures $T_1 \approx 110$ K and $T_2 \approx 220$ K. The transition at T_1 is associated with the Fe(1) sublattice (the Fe atom near the vdW gap, see Figure 1c), which remains magnetically ordered below 110 K but undergoes strong fluctuations in the intermediate temperature range.^[33,51] Previously, a magnetostuctural phase transition from a metastable phase to a stable phase has been reported in FGT.^[27] However, this transition only occurs during the initial cooling process and remains permanent.^[27] Consequently, the magnetic transition at T_1 in our sample cannot be attributed to this phenomenon, as the measurement was performed starting from a low temperature of 4.3 K. The magnetic transition at T_2 is likely associated with the change in magnetic ordering of Fe(2).^[33,51] A minor contribution may also arise from the presence of the Fe₃GeTe₂ phase. However, given its small fraction, the magnetism should be predominantly governed by the FGT phase, as further supported by transport measurements (see next section). The ferromagnetism above T_2 is primarily attributed to the long-range ferromagnetic order of Fe(3).^[33,51] This gradual change in the magnetic ordering of different Fe sublattices may also explain the slow decay of FGT magnetization at high temperatures (e.g., above 250 K in Figure 3b). In contrast, the 2D ferromagnets Fe₃GeTe₂^[3,34] and Fe₃GaTe₂^[36] do not exhibit anomalous magnetic transitions in their $M - T$ and dM/dT curves, which is consistent with the absence of reported evidence for distinct sublattice-specific ordering transitions. This behavior aligns with the sharp decrease in magnetization observed in Fe₃GeTe₂^[3,34] and Fe₃GaTe₂^[36] near their T_C . Consequently, these anomalies in temperature-dependent magnetic properties constitute a unique characteristic of FGT, with their occurrence indicating the high-quality formation of the expected FGT phase. This conclusion is further substantiated by the observation that the T_1 reported in various FGT samples remains consistent irrespective of synthesis methods of epitaxy or exfoliation.^[41-43] The successful realization of epitaxial FGT films on a TMDC template that exhibit PMA without compromising T_C offers a highly promising platform for the advancement of 2D spintronics.

2.3 Anomalous Hall effect (AHE)

To further investigate the magnetic and transport behaviors, AHE measurements were performed due to their high sensitivity to magnetization in ultrathin films.^[64] Large-area Hall-bar devices, benefiting from our scalable synthesis, were used (Figure S7, Supporting Information). **Figure 4a,b** displays the AHE curves of a 6 nm thick FGT/WSe₂ heterostructure, with low- and high-temperature data presented separately due to different AHE amplitudes. At low temperatures (Figure 4a), the square-shaped AHE loops originate from the FGT layer and confirm the presence of strong PMA. The absence of kink-like features in the AHE data indicates that the zero-coercivity component in the SQUID signal (green curve, Figure 3a) likely arises from the insulating surface oxide, previously reported to be antiferromagnetic.^[65] As oxidation is difficult to avoid entirely, even with a protective capping layer, this result highlights the complementary roles of AHE and SQUID measurements: the former selectively probes the conductive FGT layer, while the latter captures the magnetic response of the entire sample. At high temperature (Figure 4b), the AHE loops become rounded with reduced coercivity, indicating a transition from hard to soft ferromagnetism. The AHE signal vanishes near 340 K, above which only a linear ordinary Hall effect (OHE) remains.

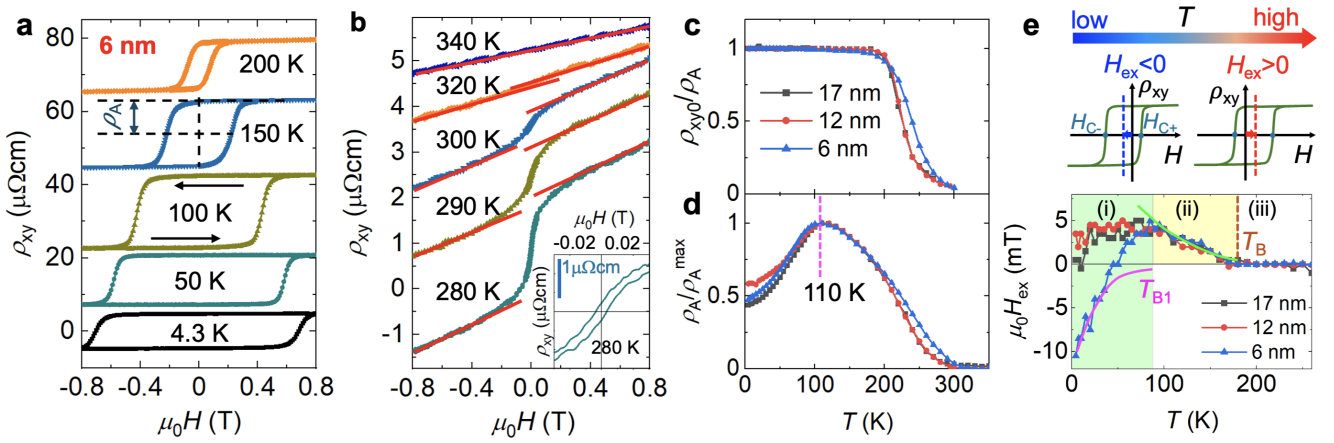


Figure 4: AHE and exchange bias effect in FGT/WSe₂ vdW heterostructures. a,b) Hall resistivity (ρ_{xy}) measured during upward and downward sweeps of the OP magnetic field at different temperatures, with sweep directions indicated by black arrows. The red lines in (b) are guides to the eye for the linear dependence in the saturation region. c,d) Temperature-dependent ρ_{xy0}/ρ_A and ρ_A/ρ_A^{max} for samples with different FGT thicknesses, where ρ_{xy0} is the zero-field ρ_{xy} and ρ_A^{max} is the maximum ρ_A . e) Top: Schematic of the sign reversal of the exchange bias controlled by temperature. Bottom: Temperature-dependent H_{ex} , with pink and green lines guiding the interfacial and bulk exchange coupling contributions, respectively.

Figure 4c displays the normalized remanent AHE resistivity, ρ_{xy0}/ρ_A , as a function of temperature for samples with different FGT thicknesses, where ρ_{xy0} and ρ_A are the AHE resistivities at zero and saturation fields (at 0.8 T with the OHE contribution subtracted), respectively. The ρ_{xy0}/ρ_A remains constant up to approximately 200 K and then gradually decreases, however sustaining magnetic order up to 300 K. Figure 4d shows the temperature-dependent ρ_A/ρ_A^{max} , where ρ_A^{max} represents the maximum value of ρ_A obtained at $T_1 = 110$ K. Below 110 K, the increase in ρ_A with increasing temperature can be mainly attributed to transport mechanisms, including intrinsic contribution of Berry curvature and extrinsic phonon-enhanced spin-dependent scattering.^[51,64] At 110 K, the peak in ρ_A is attributed to the magnetic unordering of Fe(1), while the subsequent decline at higher temperatures reflects the progressive reduction in overall magnetization.^[27,51] Combining SQUID (Figure 3) and AHE (Figure 4a-d) results, we estimate that the T_C of our FGT/WSe₂ heterostructures lies slightly above room temperature, with negligible dependence on FGT thickness. Notably, the T_C obtained in our epitaxial samples is comparable to the values reported for exfoliated FGT flakes (≈ 270 - 310 K).^[27,42] Furthermore, the T_1 temperature (110 K) determined from ρ_A^{max} agrees well with that of bulk materials^[51] and, in our case, is identical

for all samples (Figure 4d). This indicates that the Fe(1) unordering temperature is robust and not strongly dependent on film thickness.

2.4 Sign reversal of exchange bias effect

The exchange bias effect involving 2D ferromagnets has emerged as a compelling research topic due to its fundamental significance and promising spintronic applications.^[20,22,24–26] Unexpectedly, an exchange bias effect is observed in our FGT/WSe₂ heterostructures at low temperatures after cooling without additional field (see Methods), manifesting as a clear shift of the AHE loops' center from zero field, as schematically illustrated in the top panel of Figure 4e. The bottom panel of Figure 4e displays the extracted exchange bias field (H_{ex}) as a function of temperature for FGT films of different thicknesses, where $H_{\text{ex}} = (H_{\text{C}+} + H_{\text{C}-})/2$ with $H_{\text{C}\pm}$ denoting the positive and negative coercive fields, respectively (see Figures S8 and S9, Supporting Information). Remarkably, H_{ex} exhibits a sign reversal between negative and positive depending on both temperature and FGT thickness, a highly unusual behavior rarely reported in conventional 3D magnetic systems. Three distinct regimes can be identified: (i) a thickness-dependent H_{ex} below 80 K with a positive temperature coefficient, (ii) a thickness-independent positive H_{ex} between 80 and 160 K with a negative temperature coefficient, and (iii) a vanishing H_{ex} above the Blocking temperature (T_B) of 160 K. The thickness-dependent H_{ex} dominant in region (i) likely originates from an interfacial exchange bias, consistent with Meiklejohn–Bean (MB) model with a negative $H_{\text{ex}} \propto 1/t_{\text{FGT}}$.^[66–69] This interfacial exchange bias may arise from the exchange coupling at the O-FGT/FGT interface, where an antiferromagnetic order and an induced exchange bias effect have been reported in naturally oxidized Fe₅GeTe₂,^[65] Fe₃GeTe₂^[20,70] and Fe₃GaTe₂.^[71] Although our films do not show a distinct interface that would clearly distinguish oxidized and non-oxidized FGT regions in STEM characterizations, the possibility of non-uniform oxidation across the layers cannot be excluded. In contrast, the positive H_{ex} in region (ii) cannot be fully explained by the conventional exchange bias theory.^[66–69] Instead, considering the thickness independence of both H_{ex} and T_B in this temperature region, this behavior likely arises from the intrinsic bulk properties of FGT. Indeed, a positive H_{ex} has recently been observed in Fe₃GeTe₂ flakes and was attributed to the coexistence of stable and frustrated magnetism at the sublayer surface.^[72] This suggests that the positive H_{ex} may be intrinsically associated with the 2D nature of FGT.^[72,73] Consequently, the unusual exchange bias can be attributed to the interplay between two contributions: a negative H_{ex} occurring at the O-FGT/FGT interface with an estimated $T_{B1} \approx 100$ K (pink line in Figure 4e), and a positive H_{ex} emerging from the interaction between FGT sublayers with a $T_B = 160$ K (green line in Figure 4e). However, a comprehensive understanding of this unconventional exchange bias remains elusive.^[22,72,73] The complex structural and magnetic properties of O-FGT/FGT are likely sensitive to factors such as the oxidation degree, the chemical composition and the local electronic structure,^[70,73,74] which require a systematic study beyond the scope of this paper. Nevertheless, it can be anticipated that the exchange bias in our FGT samples can be further tuned by precise control of O-FGT formation (e.g., controlling air exposure time, intently introducing O₂ and growing adjacent oxide layer^[65,70]). Finally, this intrinsic, single-material-induced self-exchange bias with a tunable sign provides a unique platform for exploring interfacial magnetism and developing 2D spintronic devices.

2.5 In-plane Magnetotransport

To gain a deeper insight into the magnetic anisotropy in FGT, magnetotransport measurements were also performed by applying an in-plane magnetic field (H_{\parallel}), as illustrated in **Figure 5a**.^[9] In this configuration, the magnetization vector (pink arrows in Figure 5a) continuously moves from the OP to IP direction as H_{\parallel} increases, settling at an angle (θ) determined by the free energy

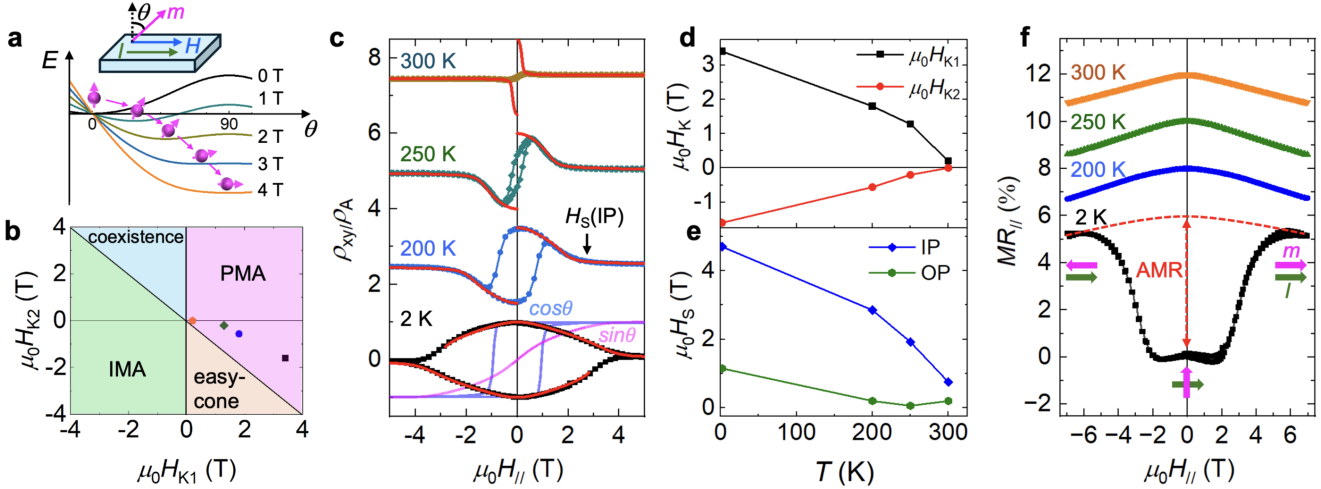


Figure 5: In-plane magnetotransport properties of a 6-nm-thick FGT/WSe₂ vdW heterostructure. a) Schematic of magnetization reorientation (pink arrows with spheres) in a PMA material under an applied in-plane magnetic field H_{\parallel} , determined by the minima of the free-energy profile (colored curves). Inset: measurement configuration. b) Phase diagram of possible magnetic states as functions of H_{K1} and H_{K2} , symbols mark values extracted from the fits in c). c) ρ_{xy}/ρ_A versus H_{\parallel} , with ρ_A obtained from AHE measurements (Figure 4). The red curves are fits based on Equation (2). d) Temperature dependence of H_{K1} and H_{K2} extracted from fits in c). e) Temperature dependence of H_S obtained from AHE loops with OP (Figure 4a,b) and IP (see estimation in c) field orientations. f) In-plane longitudinal magnetoresistance MR_{\parallel} versus H_{\parallel} at different temperatures; the red line indicates the method used to estimate the AMR value.

landscape $E(\theta)$:^[9,75,76]

$$E = -\frac{1}{2}\mu_0 H_{K1} M_S \cos^2 \theta - \frac{1}{4}\mu_0 H_{K2} M_S \cos^4 \theta - \mu_0 H_{\parallel} M_S \cos(\theta_H - \theta) \quad (2)$$

Here, H_{K1} and H_{K2} denote the first- and second-order PMA fields, respectively, while θ_H represents a slight misalignment (less than 2°, see Methods) of the applied H_{\parallel} relative to the film plane. The equilibrium magnetization state is obtained at the minima of $E(\theta)$. The phase diagram in Figure 5b shows the accessible magnetic states by tuning H_{K1} and H_{K2} (see Figure S10, Supporting Information). Figure 5c presents the ρ_{xy}/ρ_A as a function of H_{\parallel} measured at different temperatures for the 6 nm FGT/WSe₂ heterostructure. Due to I/H_{\parallel} (Figure 5a), both the OHE and the planar Hall effect (PHE) are excluded, resulting in $\rho_{xy} \propto M_{\perp}$ and $\cos \theta = \rho_{xy}/\rho_A$. At low temperatures (2 and 200 K), a monotonic increase of ρ_{xy}/ρ_A with decreasing H_{\parallel} from high field indicates a coherent rotation of the magnetization from IP to OP direction, further resulting in identical ρ_{xy0} values for both OP and IP field sweeps. At elevated temperatures (250 and 300 K), the weaker PMA leads to a large number of multi-domain states forming near zero field, consequently reducing the net magnetization and ρ_{xy} . Furthermore, we extracted $\cos \theta(H_{\perp}) = \rho_{xy}(H_{\perp})/\rho_A$ (blue curve) and $\sin \theta(H_{\parallel}) = \sqrt{1 - [\rho_{xy}(H_{\parallel})/\rho_A]^2}$ (pink curve) at 2 K (Figure 5c), corresponding to M_{\perp} versus H_{\perp} and M_{\parallel} versus H_{\parallel} , respectively. The square and linear trends of these curves align with the SQUID data (Figure 3a). These results strongly confirm a robust, uniaxial PMA without metastable tilted states.

For quantitative analysis, ρ_{xy}/ρ_A was fitted (red lines, Figure 5c) using the macrospin model of Equation (2) (see Methods), valid in the single domain regime when the field decreases from a high field. Our analysis indicates that a higher-order PMA term (H_{K2}) is essential to adequately capture the experimental response. Figure 5d displays the extracted H_{K1} and H_{K2} as a function of temperature. Both decrease monotonically due to thermal fluctuations,^[9] yet remaining within the uniaxial PMA regime far from phase boundaries (symbols, Figure 5b). These findings underscore the robustness of PMA over a wide temperature range. The emergence of higher-order PMA is likely due to the presence of multiple Fe sublattices in FGT, each experiencing distinct SOC and crystal field environments.^[52,77] This microscopic complexity aligns with the rich magnetic behav-

ions observed in FGT, including PMA-IMA transitions,^[41] canted phases^[9,78] and non-collinear spin order^[27]. In contrast, Fe_3GeTe_2 and Fe_3GaTe_2 , which possess fewer Fe sites, exhibit a simpler magnetic behavior, exclusively characterized by PMA and devoid of temperature-induced phase transitions.^[3,34,36] Meanwhile, the SOC in FGT is predominantly attributed to the Te atoms, while the Fe d-orbitals contribute moderate SOC strength.^[52,77] This aligns with the observation that Fe_3GeTe_2 and Fe_3GaTe_2 , which possess a higher Te/Fe ratio and thus enhanced SOC, exhibit stronger PMA than FGT.^[34,36,44] Nevertheless, the more complex PMA landscape in FGT offers enhanced tunability of magnetic properties, offering a distinct advantage for tailoring magnetization dynamics, such as field-free SOT switching.^[13,79,80] Finally, Figure 5e compares the saturation fields H_S obtained from AHE measurements with IP (see estimation in Figure 5c) and OP (Figure 4a,b) fields. A significantly smaller H_S in the OP direction confirms the PMA up to room temperature, consistent with previous results from AHE (Figure 4a-d) and SQUID (Figure 3) characterizations.

Figure 5f shows the in-plane longitudinal magnetoresistance, defined as $MR_{\parallel} = [\rho_{xx}(H_{\parallel}) - \rho_{xx}(0 \text{ T})]/\rho_{xx}(0 \text{ T}) \times 100\%$, with the indicated magnetization (pink arrows) and current (green arrows) directions. At 2 K, the positive MR_{\parallel} observed in a large field ($M \parallel I$) compared to zero field ($M \perp I$) arises from the AMR effect. The extracted AMR of 5.8% (definition in Figure 5f) notably exceeds that of Fe_3GeTe_2 under similar conditions.^[81] Given that AMR is typically correlated with the SOC strength,^[82] this result is unexpected due to a weaker SOC in FGT than Fe_3GeTe_2 . However, the AMR response in FGT may reflect the unequal contributions of its multiple Fe sublattices. Among them, Fe(1) experiences stronger SOC due to hybridization between the Fe 3d and Te 5p orbitals with a larger orbital magnetic moment.^[52] The pronounced AMR observed in FGT can thus be primarily attributed to Fe(1), whose contribution dominates the spin-dependent scattering. This hypothesis is further supported by structural data: the Te–Fe(1) bond length in FGT (2.61 Å) is shorter than that in Fe_3GeTe_2 (2.73 Å),^[72] likely enhancing SOC at Fe(1) and contributing to the higher AMR in FGT. The temperature dependence of AMR further corroborates this perspective. Above 200 K, the AMR becomes negligible, despite only modest changes in both M and ρ_A (Figure 3b and 4c-d). This discrepancy may suggest that the significant suppression of AMR does not arise from reduced magnetization, but rather from magnetic unordering of Fe(1), leading to a diminished SOC-mediated scattering contribution. This assertion is further substantiated by the observation that ρ_A exhibits a decline around 110 K (Figure 4d), a temperature much lower than the 0.75 T_C threshold expected for a magnetization-driven decrease.^[64,83] Collectively, these observations suggest that carrier transport in FGT is predominantly governed by spin-dependent scattering at Fe(1), which exhibits substantial SOC, while the contributions from Fe(2) and Fe(3) remain limited due to their weaker SOC.

2.6 Thickness-dependent unconventional Hall effect

To evaluate the potential formation of topological magnetic orders in our FGT/WSe₂ heterostructures, the AHE measurements were further performed using a high-resolution setup, as shown in **Figure 6a** for a 17 nm FGT/WSe₂ sample measured at 4.3 K. Indeed, a clear unconventional Hall effect (UHE) was observed during both forward and backward field sweeps (highlighted shaded regions), deviating from the conventional AHE baseline (red curves). Additional UHE results for different Hall devices and temperatures can be found in our previous report.^[84] Three distinct deviations with characteristic up-down-up features are consistent with topological Hall effect (THE) signatures arising from topological spin textures^[30,32,85,86], well matching theoretical predictions for the influences of skyrmions and antiskyrmions on Hall signals.^[85] In fact, the skyrmion formation and corresponding THE are highly expected in FGT/WSe₂ heterostructures due to their intrinsic magnetic properties and the potential influence of interfacial proximity effects.^[27,30,32,86] Importantly, the possibility that the observed AHE anomalies arise from additional magnetic phases can be confidently excluded. For this hypothesis to be valid, the hypothetical secondary phase must produce an AHE with a sign opposite to FGT, thereby requiring distinct Berry curvatures. How-

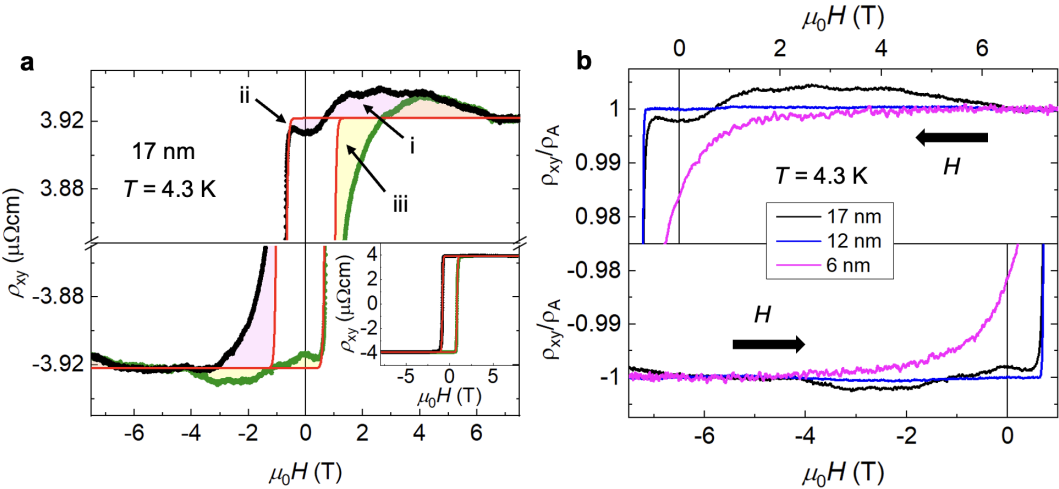


Figure 6: Unconventional Hall effect (UHE) in FGT/WSe₂ vdW heterostructures. a) $\rho_{xy} - H$ of a 17 nm FGT/WSe₂ sample at 4.3 K with downward (black) and upward (green) field sweeps after subtraction of the linear OHE contribution. The red curves represent the assumed conventional AHE component, and the shaded regions highlight the unconventional contributions. Inset: full $\rho_{xy} - H$ loop showing the sharp magnetization switching. b) Thickness dependence of the UHE. For clarity, only the curves obtained while reducing the magnetic field from high values are shown, with sweep direction indicated by black arrows.

ever, such a phase would manifest as distinct magnetic behavior, including different coercive fields and multi-step, narrow-waist magnetization switching. In contrast, the full-range loops exhibit sharp single-step switching (inset in Figure 6a), without indication of multiple discrete transitions. This conclusion is further supported by in-plane field measurements (Figure 5c), which demonstrates a continuous and seamless rotation of the magnetization from IP to OP directions. These findings may suggest the formation of skyrmions within our FGT/WSe₂ heterostructures, with the observed UHE attributed to THE. We anticipate that further enhancement and clearer observation of THE will be achievable in nanoscale Hall bar devices with lateral dimensions comparable to skyrmion sizes. Combined with skyrmion imaging, this approach could enable detailed studies of skyrmion–carrier interactions, which we plan to pursue systematically in future work.

To investigate the influence of WSe₂ on UHE, we systematically examined its dependence on FGT thickness. For clarity, Figure 6b only presents the curves recorded during the magnetic field sweep from high to low field, with black arrows indicating the sweep direction. In contrast to the 17 nm FGT sample (black), which exhibits a clear UHE signature, the 12 nm (blue) and 6 nm (pink) samples manifest only conventional AHE. Notably, the detection of UHE in transport measurements critically depends on the skyrmion density. A threshold density is required to produce a measurable UHE signal.^[30] According to a recent study on skyrmions in FGT, a topological Hall resistivity of 0.02 $\mu\Omega\text{cm}$ [region (i) in Figure 6a] corresponds to a skyrmion density about 1 μm^{-2} .^[30] Assuming a skyrmion size of 65 nm,^[30] this yields a ratio of 0.004 between the skyrmion area and the total FGT area. Notably, this value closely matches the ratio of the UHE and AHE signals (≈ 0.004 , Figure 6b). This consistency further supports the correlation between the UHE and skyrmion formation in our samples. Consequently, the absence of the UHE signal in thinner samples may not preclude skyrmion formation but likely indicates a lower skyrmion density compared to thicker films. These findings imply that skyrmions predominantly form within the FGT bulk rather than at the FGT/WSe₂ interface. This contrasts with Fe₃GeTe₂-based heterostructures, such as Fe₃GeTe₂/WTe₂, where skyrmions were reported to form at the heterointerface rather than within the bulk.^[86] A potential origin of this difference may lie in the different PMA strengths of Fe₃GeTe₂ and FGT. Typically, Fe₃GeTe₂ exhibits a stronger PMA,^[3,34] which favors collinear spin alignment and thus suppresses skyrmion formation. In such systems, the adjacent TMDC layer can modulate PMA to an intermediate regime that promotes non-collinear spin textures at the interface. In contrast, FGT films inherently exhibit moderate PMA strength, allowing

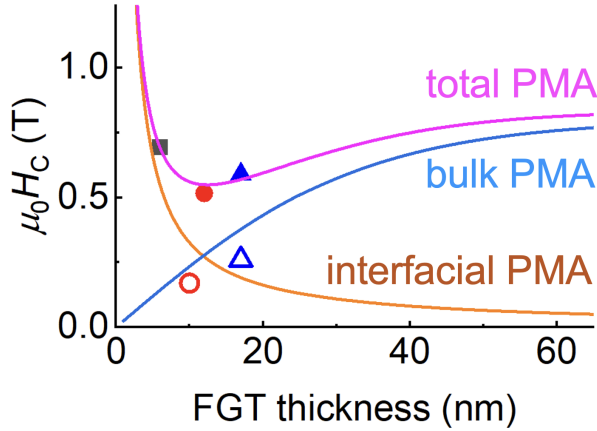


Figure 7: Non-monotonic thickness dependence of H_C in FGT/WSe₂ heterostructures (filled symbols). The data are fitted (pink curve) using Equation (3), with contributions from bulk PMA (blue curve) and interfacial PMA (orange curve). Open symbols show reference data obtained from FGT/graphene heterostructures.^[18]

skyrmion formation.^[27,30] However, the presence of WSe₂ may further enhance PMA due to its large SOC and interfacial proximity effects, potentially impeding skyrmion nucleation in thinner FGT. Therefore, PMA acts as a key parameter for controlling the balance between collinear and non-collinear spin configurations, critically influencing skyrmion formation. This provides FGT with a distinct advantage over Fe₃GeTe₂ on skyrmion creation. Moreover, while interfacial skyrmions are typically 2D spin textures, skyrmions in thicker FGT layers could support more complex topological spin texture, such as 3D hopfion rings.^[87,88] This expands the landscape of accessible magnetic textures. The formation and density of skyrmions in FGT/WSe₂ heterostructures may be further manipulated by tuning temperature, magnetic field and layer thickness. In addition, skyrmions in FGT can be topologically protected, providing robust stability against external perturbations.^[27,31] These potentials make FGT/WSe₂ heterostructures a compelling platform for skyrmion research and applications, including the skyrmion Hall effect,^[89] skyrmion-based racetrack memory^[90,91] and neuromorphic computing^[92].

2.7 Proximity-induced interfacial contributions to magnetic and transport anomalies

To further investigate the influence of WSe₂ on the magnetic and transport properties of FGT, we examined the thickness dependence of H_C for FGT films (taken from AHE curves in Figure 4a at 4.3 K) grown on epitaxial WSe₂ and, as a reference, on epitaxial graphene.^[18,84,93] Unlike the monotonic behavior typically reported for exfoliated FGT flakes,^[44,94] H_C in FGT/WSe₂ exhibits an unconventional non-monotonic dependence on t_{FGT} (Figure 7, filled symbols). This behavior can be well described by considering both bulk and interfacial PMA contributions:^[44]

$$H_C = H_{C0} \tanh\left(\frac{2t_{\text{FGT}}}{t_0}\right) + \frac{J_{\text{int}}}{M_S t_{\text{FGT}}} \quad (3)$$

The first term, saturating at H_{C0} for $t_{\text{FGT}} > t_0$, describes bulk PMA with a feature typically reported in 2D ferromagnet flakes.^[44,94] The second term, proportional to $1/t_{\text{FGT}}$, captures interfacial PMA from interlayer coupling at the FGT/WSe₂ interface. Fitting yields $t_0 = 66$ nm, consistent with values reported for Fe₃GeTe₂ (≈ 60 nm),^[44] and $J_{\text{int}} \approx 1.0$ mJ/m², comparable to conventional interfacial PMA systems such as Co/Pt ($0.6 \sim 1.4$ mJ/m²)^[37,95,96] and CoFeB/MgO (1.8 mJ/m²).^[37,97] The pronounced $1/t_{\text{FGT}}$ term reveals a strong interface-driven enhancement of PMA. In 3D ferromagnet/heavy-metal and ferromagnet/oxide systems, the interfacial PMA typically originates from SOC-mediated hybridization at the interface.^[37,39,40] By analogy, our results strongly indicate that the interfacial PMA in FGT/WSe₂ is attributed to SOC from the WSe₂ underlayer — a signature of a proximity effect. This interpretation is further supported by the consistently higher H_C in FGT/WSe₂ (filled symbols, Figure 7) compared to FGT/graphene

(open symbols, Figure 7), despite similar crystalline quality,^[18,84,93] in line with the much stronger SOC in WSe₂ than in graphene. Furthermore, our results align well with previous reports of proximity-induced enhancement of H_C through TMDC integration.^[98] The non-monotonic PMA profile, arising from the competition between bulk and interfacial contributions, is a distinctive feature of vdW heterostructures. In contrast, exfoliated FGT flakes exhibit only the bulk term,^[44,94] while 3D ferromagnet/heavy-metal and ferromagnet/oxide systems show only the interfacial contribution.^[37] This integration provides enhanced tunability of magnetic anisotropy, which could be further modulated via the WSe₂ thickness. Overall, the thickness scaling, quantitative fits, comparison between FGT/WSe₂ and FGT/graphene, as well as SOC considerations provide strong evidence that the magnetic and transport anomalies (e.g, unusual thickness dependence of UHE and PMA) in our FGT/WSe₂ heterostructures arise from an interfacial SOC-driven proximity effect, enabled by the clean and atomically sharp nature of the interface. This tunability establishes FGT/WSe₂ as a promising platform for studying proximity-driven physics.

3 Conclusion

In this work, we have demonstrated the realization of large-scale, all-epitaxial FGT/WSe₂ vdW heterostructures exhibiting unconventional magnetic and transport properties unique to their 2D nature. Large-area synthesis using MBE and CVD enables us to overcome the scalability challenge, achieving ferromagnetic/semiconducting vdW heterostructures that exhibit room temperature ferromagnetism. This marks a significant advance in the realization of 2D magnetic systems for device integration. The FGT/WSe₂ heterostructures exhibit PMA while maintaining the T_C , which is beneficial for low-power spintronic applications. The unusual thickness- and temperature-dependent sign reversal of exchange bias highlights distinctive 2D magnetic behavior. In-plane magneto-transport further reveals a pronounced higher-order PMA contribution and unusually large AMR effect, pointing to sublattice-specific roles in governing magnetism and transport unique to FGT. The reversed thickness dependence of the UHE, opposite to trends reported for Fe₃GeTe₂-based heterostructures, underscores the interplay between PMA and interfacial coupling, suggesting the possible formation of skyrmions. Together with the non-monotonic PMA-thickness dependence, these magnetic and transport anomalies can be attributed to a strong interfacial proximity effect at the FGT/WSe₂ interface, enabled by the high epitaxial quality and the strong SOC of WSe₂. These heterostructures establish a robust and versatile platform for both fundamental studies and next-generation 2D spintronic technologies, including vdW magnetoresistive devices, ultrahigh-density racetrack memories and proximity-engineered magnetic functionalities.

Experimental Section

MBE growth: FGT was grown by MBE using elemental Fe, Ge, and Te evaporated from Knudsen cells. The flux for each element was obtained by measuring the beam equivalent pressure employing a pressure gauge. For the flux ratios utilized in this study, the average composition of the films is Fe_{4.8}GeTe₂.^[18] Continuous films with thicknesses of around 6, 12, and 17 nm were prepared at a substrate temperature of 260 °C. In-situ growth monitoring was performed by RHEED. As growth templates, we used single-crystalline, continuous monolayer–bilayer thick WSe₂ films synthesized on Al₂O₃(0001) by CVD. Details about the CVD growth of WSe₂ can be found elsewhere.^[47] Prior to FGT growth, the 1 cm² large WSe₂/Al₂O₃(0001) templates (cut out of 2-inch wafers) were in situ annealed at 300 °C for 20 minutes in order to remove surface contaminants. The FGT films were capped in-situ after their growth with a Te layer (5 nm) deposited after sample cooling to room temperature. This procedure was adopted in order to minimize FGT surface oxidation upon air exposure. This provided additional protection against FGT oxidation during transportation of the samples from the MBE laboratory in Germany to the STEM laboratory in Spain.

Grazing incidence diffraction: Measurements shown in Figure 1 were performed at beamline P23 at PETRA III using an X-ray energy of 18 keV. Experiments shown in Figure S3 (Supporting Information) were performed at the BM25- SpLine beamline at The European Synchrotron (ESRF) in Grenoble. An incidence angle of the illuminating X-rays of 0.2° sufficiently suppresses strong scattering by the substrate, and thus makes this method highly surface sensitive. An X-ray wavelength of 0.689 \AA (corresponding to a photon energy of 18 keV), selected by a Si(111) monochromator, enables inspection of a comparatively large area in reciprocal space, which is important for accessing multiple reflections of the same lattice plane family.

Scanning transmission electron microscopy (STEM) and electron energy loss spectroscopy (EELS): An electron transparent TEM lamella was prepared in a Dual Beam Helios 5 UX Focused ion beam. Atomic-resolution high-angle annular dark-field (HAADF) STEM images were acquired in a double-corrected ThermoFisher SPECTRA 300 (S)TEM microscope operated at 200KV. For the image acquisitions, a convergence and collection semiangles of around 20 mrad and 67-200 mrad were used. EELS spectrum images were acquired using a continuum spectrometer from GATAN, equipped with the K3 direct electron detection camera and operated in counted mode, 40-50 mrad collection angle, 20 pm pixel size, 70 pA probe current and 2 ms dwell time.

Magnetic characterization: The magnetic properties of the FGT/WSe₂ films were characterized using a SQUID magnetometer (Quantum Design MPMS-3) under vacuum with magnetic fields up to 5 T. Hysteresis loops (Figure 3a) were acquired by sweeping the external magnetic field, and a linear diamagnetic background was subtracted (Figure S5, Supporting Information). For the $M-T$ measurements (Figure 3b), the samples were first cooled to 4 K in zero field, after which the magnetization was initialized using a 1 T field. The field was then reduced to zero, and the $M-T$ curves were recorded during subsequent zero-field warming. All measurements were performed for both out-of-plane (OP) and in-plane (IP) field configurations.

Hall device fabrication: Thin FGT/WSe₂ films were patterned into Hall bar devices using standard cleanroom fabrication techniques. Since Ar⁺ plasma etching makes the photoresist difficult to remove, the electrodes were first defined by optical lithography, followed by electron beam evaporation of Cr (9 nm)/Au (80 nm). The Hall bar structures were then defined through a second optical lithography step and Ar⁺ ion-beam etching. To prevent peeling of vdW layers during photoresist removal, a hot acetone bath at 50 °C was employed instead of the conventional lift-off process. Finally, the fabricated Hall devices were wire-bonded to a chip carrier using Al wires. Figure S7 (Supporting Information) displays an image of fabricated Hall device, with a width of 100 μm and a length between two arms of 300 μm .

Magnetotransport: AHE measurements (Figure 4) were performed on Hall bar devices (Figure S7, Supporting Information) under external out-of-plane magnetic fields up to 0.8 T in vacuum conditions (10^{-6} to 10^{-7} mbar). The AHE loops were initially measured at room temperature, followed by zero-field cooling to 4.3 K. Subsequent AHE curves were measured at each temperature from 4.3 to 400 K. A constant direct current (DC) was applied using a Hewlett-Packard 3245A current source, while Hall voltage was measured using a Hewlett-Packard 3458A digital multimeter. In-plane transport measurements (Figure 5) were performed with an in-plane field up to 7 T parallel to the current direction (see Figure 5a) from 2 to 300 K. UHE measurements (Figure 6) were performed in an Attocube system with an out-of-plane field up to 8 T and a lock-in detection (SR 830) at a frequency of ≈ 37 Hz.

Data simulation: For the analysis of the in-plane transport data (Figure 5c), the stable magnetization state was obtained from Equation (2) under the conditions of $\partial E/\partial\theta = 0$ and $\partial^2 E/\partial\theta^2 > 0$, resulting in:

$$H_{K1} \cos\theta \sin\theta + H_{K2} \cos^3\theta \sin\theta = H_{\parallel} \sin(\theta_H - \theta) \quad (4)$$

The transport data were fitted using Mathematica, as shown by red curves in Figure 5c. The best fit results in $\theta_H \approx 88^\circ$, indicating a slight $\approx 2^\circ$ deviation of the applied field from the film plane.

See also Figures S11, Supporting information. For the analysis of thickness-dependent H_C using Equation (3) (Figure 7), we used $M_S = 308 \text{ emu/cm}^3$ estimated from SQUID measurements in the saturation regime (4–5 T in Figure 3a). Fitting the data yields $J_{\text{int}} \approx 1.0 \text{ mJ/m}^2$, $t_0 = 66 \text{ nm}$ and $H_{C0} = 0.8 \text{ T}$.

Supporting Information

Supporting Information is available from the Wiley Online Library or from the author.

Acknowledgements

We thank Dr. A. Khadiev and Dr. D. Novikov for their support during setting up the experiment. We also acknowledge PETRA III for providing beamtime through proposal I-20230728. We thank the ESRF for providing beamtime through proposal HC-6285 and Dr. Juan Rubio Zuazo for his assistance during the experimental setup. Authors acknowledge the use of instrumentation as well as the technical advice provided by the Joint Electron Microscopy Center at ALBA (JEMCA) and funding from Grant IU16-014206 (METCAM-FIB) to ICN2 funded by the European Union through the European Regional Development Fund (ERDF), with the support of the Ministry of Research and Universities, Generalitat de Catalunya. Authors acknowledge Marcos Rosado for the lamella preparation. The group in Mainz acknowledges the German Research Foundation (DFG SFB TRR173 Spin+X 268565370, projects A01, B02 and A12 and DFG SFB TRR288 ELASTO-Q-MAT 422213477, projects A09 and A12), the European Union’s Horizon 2020 Research and Innovation Programme under grant agreement 856538 (project “3D MAGIC”) and King Abdullah University of Science and Technology (KAUST) under award 2024-CRG12-6480.

References

- [1] C. Gong, L. Li, Z. Li, H. Ji, A. Stern, Y. Xia, T. Cao, W. Bao, C. Wang, Y. Wang, Z. Q. Qiu, R. J. Cava, S. G. Louie, J. Xia, X. Zhang, Discovery of intrinsic ferromagnetism in two-dimensional van der Waals crystals, *Nature* **2017**, *546*, 7657 265.
- [2] B. Huang, G. Clark, E. Navarro-Moratalla, D. R. Klein, R. Cheng, K. L. Seyler, D. Zhong, E. Schmidgall, M. A. McGuire, D. H. Cobden, W. Yao, D. Xiao, P. Jarillo-Herrero, X. Xu, Layer-dependent ferromagnetism in a van der Waals crystal down to the monolayer limit, *Nature* **2017**, *546*, 7657 270.
- [3] Z. Fei, B. Huang, P. Malinowski, W. Wang, T. Song, J. Sanchez, W. Yao, D. Xiao, X. Zhu, A. F. May, W. Wu, D. H. Cobden, J.-H. Chu, X. Xu, Two-dimensional itinerant ferromagnetism in atomically thin Fe_3GeTe_2 , *Nat. Mater.* **2018**, *17*, 9 778.
- [4] J. Seo, D. Y. Kim, E. S. An, K. Kim, G.-Y. Kim, S.-Y. Hwang, D. W. Kim, B. G. Jang, H. Kim, G. Eom, S. Y. Seo, R. Stania, M. Muntwiler, J. Lee, K. Watanabe, T. Taniguchi, Y. J. Jo, J. Lee, B. I. Min, M. H. Jo, H. W. Yeom, S.-Y. Choi, J. H. Shim, J. S. Kim, Nearly room temperature ferromagnetism in a magnetic metal-rich van der Waals metal, *Sci. Adv.* **2020**, *6*, 3 eaay8912.
- [5] T. Song, X. Cai, M. W.-Y. Tu, X. Zhang, B. Huang, N. P. Wilson, K. L. Seyler, L. Zhu, T. Taniguchi, K. Watanabe, M. A. McGuire, D. H. Cobden, D. Xiao, W. Yao, X. Xu, Giant tunneling magnetoresistance in spin-filter van der Waals heterostructures, *Science* **2018**, *360*, 6394 1214.
- [6] H. Yang, S. O. Valenzuela, M. Chshiev, S. Couet, B. Dieny, B. Dlubak, A. Fert, K. Garello, M. Jamet, D.-E. Jeong, K. Lee, T. Lee, M.-B. Martin, G. S. Kar, P. Sénéor, H.-J. Shin, S. Roche, Two-dimensional materials prospects for non-volatile spintronic memories, *Nature* **2022**, *606*, 7915 663.

[7] B. Huang, M. A. McGuire, A. F. May, D. Xiao, P. Jarillo-Herrero, X. Xu, Emergent phenomena and proximity effects in two-dimensional magnets and heterostructures, *Nat. Mater.* **2020**, *19*, 12 1276.

[8] M. Gibertini, M. Koperski, A. F. Morpurgo, K. S. Novoselov, Magnetic 2D materials and heterostructures, *Nat. Nanotechnol.* **2019**, *14*, 5 408.

[9] M. Tang, J. Huang, F. Qin, K. Zhai, T. Ideue, Z. Li, F. Meng, A. Nie, L. Wu, X. Bi, C. Zhang, L. Zhou, P. Chen, C. Qiu, P. Tang, H. Zhang, X. Wan, L. Wang, Z. Liu, Y. Tian, Y. Iwasa, H. Yuan, Continuous manipulation of magnetic anisotropy in a van der Waals ferromagnet via electrical gating, *Nat. Electron.* **2023**, *6*, 1 28.

[10] Z. Zhang, R. Sun, Z. Wang, Recent Advances in Two-Dimensional Ferromagnetic Materials-Based van der Waals Heterostructures, *ACS Nano.* **2025**, *19*, 1 187.

[11] Y.-C. Lin, R. Torsi, R. Younas, C. L. Hinkle, A. F. Rigos, H. M. Hill, K. Zhang, S. Huang, C. E. Shuck, C. Chen, Y.-H. Lin, D. Maldonado-Lopez, J. L. Mendoza-Cortes, J. Ferrier, S. Kar, N. Nayir, S. Rajabpour, A. C. T. Van Duin, X. Liu, D. Jariwala, J. Jiang, J. Shi, W. Mortelmans, R. Jaramillo, J. M. J. Lopes, R. Engel-Herbert, A. Trofe, T. Ignatova, S. H. Lee, Z. Mao, L. Damian, Y. Wang, M. A. Steves, K. L. Knappenberger, Z. Wang, S. Law, G. Bepete, D. Zhou, J.-X. Lin, M. S. Scheurer, J. Li, P. Wang, G. Yu, S. Wu, D. Akinwande, J. M. Redwing, M. Terrones, J. A. Robinson, Recent Advances in 2D Material Theory, Synthesis, Properties, and Applications, *ACS Nano.* **2023**, acsnano.2c12759.

[12] S. Jiang, L. Li, Z. Wang, J. Shan, K. F. Mak, Spin tunnel field-effect transistors based on two-dimensional van der Waals heterostructures, *Nat. Electron.* **2019**, *2*, 4 159.

[13] A. Fert, R. Ramesh, V. Garcia, F. Casanova, M. Bibes, Electrical control of magnetism by electric field and current-induced torques, *Rev. Mod. Phys.* **2024**, *96*, 1 015005.

[14] M. Kuepferling, A. Casiraghi, G. Soares, G. Durin, F. Garcia-Sanchez, L. Chen, C. Back, C. Marrows, S. Tacchi, G. Carlotti, Measuring interfacial Dzyaloshinskii-Moriya interaction in ultrathin magnetic films, *Rev. Mod. Phys.* **2023**, *95*, 1 015003.

[15] A. Manchon, J. Železný, I. Miron, T. Jungwirth, J. Sinova, A. Thiaville, K. Garello, P. Gambardella, Current-induced spin-orbit torques in ferromagnetic and antiferromagnetic systems, *Rev. Mod. Phys.* **2019**, *91*, 3 035004.

[16] F. Hellman, A. Hoffmann, Y. Tserkovnyak, G. S. Beach, E. E. Fullerton, C. Leighton, A. H. MacDonald, D. C. Ralph, D. A. Arena, H. A. Dürr, P. Fischer, J. Grollier, J. P. Heremans, T. Jungwirth, A. V. Kimel, B. Koopmans, I. N. Krivorotov, S. J. May, A. K. Petford-Long, J. M. Rondinelli, N. Samarth, I. K. Schuller, A. N. Slavin, M. D. Stiles, O. Tchernyshyov, A. Thiaville, B. L. Zink, Interface-induced phenomena in magnetism, *Rev. Mod. Phys.* **2017**, *89*, 2 025006.

[17] A. K. Geim, I. V. Grigorieva, Van der Waals heterostructures, *Nature* **2013**, *499*, 7459 419.

[18] H. Lv, A. da Silva, A. I. Figueroa, C. Guillemand, I. F. Aguirre, L. Camosi, L. Aballe, M. Valvidares, S. O. Valenzuela, J. Schubert, M. Schmidbauer, J. Herfort, M. Hanke, A. Trampert, R. Engel-Herbert, M. Ramsteiner, J. M. J. Lopes, Large-Area Synthesis of Ferromagnetic $Fe_{5-x}GeTe_2$ /Graphene van der Waals Heterostructures with Curie Temperature above Room Temperature, *Small* **2023**, *19*, 39 2302387.

[19] E.-M. Choi, K. I. Sim, K. S. Burch, Y. H. Lee, Emergent Multifunctional Magnetic Proximity in van der Waals Layered Heterostructures, *Adv. Sci.* **2022**, *9*, 21 2200186.

[20] Y. Wu, W. Wang, L. Pan, K. L. Wang, Manipulating Exchange Bias in a Van der Waals Ferromagnet, *Adv. Mater.* **2022**, *34*, 12 2105266.

[21] J. F. Sierra, J. Fabian, R. K. Kawakami, S. Roche, S. O. Valenzuela, Van der Waals heterostructures for spintronics and opto-spintronics, *Nat. Nanotechnol.* **2021**, *16*, 8 856.

[22] A. Puthirath Balan, A. Kumar, P. Reiser, J. Vimal Vas, T. Denneulin, K. D. Lee, T. G. Saunderson, M. Tschudin, C. Pellet-Mary, D. Dutta, C. Schrader, T. Scholz, J. Geuchies, S. Fu, H. Wang, A. Bonanni, B. V. Lotsch, U. Nowak, G. Jakob, J. Gayles, A. Kovacs, R. E. Dunin-Borkowski, P. Maletinsky, M. Kläui, Identifying the Origin of Thermal Modulation of Exchange Bias in $\text{MnPS}_3/\text{Fe}_3\text{GeTe}_2$ van der Waals Heterostructures, *Adv. Mater.* **2024**, *36*, 35 2403685.

[23] A. Kumar, S. Hameed, T. Denneulin, A. P. Balan, J. Vas, K. Leutner, L. Gao, O. Gomonay, J. Sinova, R. E. Dunin-Borkowski, M. Kläui, Switchable Exchange Bias Resulting From Correlated Domain Structures in Orthogonally Coupled Antiferromagnet/Ferromagnet van der Waals Heterostructures, *Small* **2025**, *21*, 42 e06284.

[24] T. M. J. Cham, R. J. Dorrian, X. S. Zhang, A. H. Dismukes, D. G. Chica, A. F. May, X. Roy, D. A. Muller, D. C. Ralph, Y. K. Luo, Exchange Bias Between van der Waals Materials: Tilted Magnetic States and Field-Free Spin–Orbit-Torque Switching, *Adv. Mater.* **2024**, *36*, 13 2305739.

[25] H. Xiao, B. Lyu, M. Mi, J. Yuan, X. Zhang, L. Yu, Q. Cui, C. Wang, J. Song, M. Huang, Y. Tian, L. Liu, T. Taniguchi, K. Watanabe, M. Liu, Y. Guo, S. Wang, Y. Wang, Polarity-Reversal of Exchange Bias in van der Waals $\text{FePS}_3/\text{Fe}_3\text{GaTe}_2$ Heterostructures, *Adv. Sci.* **2024**, *11*, 48 2409210.

[26] T. Zhang, Y. Zhang, M. Huang, B. Li, Y. Sun, Z. Qu, X. Duan, C. Jiang, S. Yang, Tuning the Exchange Bias Effect in 2D van der Waals Ferro-/Antiferromagnetic $\text{Fe}_3\text{GeTe}_2/\text{CrOCl}$ Heterostructures, *Adv. Sci.* **2022**, *9*, 11 2105483.

[27] M. Schmitt, T. Denneulin, A. Kovács, T. G. Saunderson, P. Rüßmann, A. Shahee, T. Scholz, A. H. Tavabi, M. Gradhand, P. Mavropoulos, B. V. Lotsch, R. E. Dunin-Borkowski, Y. Mokrousov, S. Blügel, M. Kläui, Skyrmionic spin structures in layered Fe_5GeTe_2 up to room temperature, *Commun. Phys.* **2022**, *5*, 1 254.

[28] Y. Ji, S. Yang, H.-B. Ahn, K.-W. Moon, T.-S. Ju, M.-Y. Im, H.-S. Han, J. Lee, S.-y. Park, C. Lee, K.-J. Kim, C. Hwang, Direct Observation of Room-Temperature Magnetic Skyrmion Motion Driven by Ultra-Low Current Density in Van Der Waals Ferromagnets, *Adv. Mater.* **2024**, *36*, 21 2312013.

[29] C. Liu, S. Zhang, H. Hao, H. Algaidi, Y. Ma, X.-X. Zhang, Magnetic Skyrmions above Room Temperature in a van der Waals Ferromagnet Fe_3GaTe_2 , *Adv. Mater.* **2024**, *36*, 18 2311022.

[30] X. Lv, Y. Huang, K. Pei, C. Yang, T. Zhang, W. Li, G. Cao, J. Zhang, Y. Lai, R. Che, Manipulating the Magnetic Bubbles and Topological Hall Effect in 2D Magnet Fe_5GeTe_2 , *Adv. Funct. Mater.* **2024**, *34*, 11 2308560.

[31] B. W. Casas, Y. Li, A. Moon, Y. Xin, C. McKeever, J. Macy, A. K. Petford-Long, C. M. Phatak, E. J. G. Santos, E. S. Choi, L. Balicas, Coexistence of Merons with Skyrmions in the Centrosymmetric Van Der Waals Ferromagnet $\text{Fe}_{5-x}\text{GeTe}_2$, *Adv. Mater.* **2023**, *35*, 17 2212087.

[32] H. Zhang, D. Raftrey, Y.-T. Chan, Y.-T. Shao, R. Chen, X. Chen, X. Huang, J. T. Reichenadter, K. Dong, S. Susarla, L. Caretta, Z. Chen, J. Yao, P. Fischer, J. B. Neaton, W. Wu, D. A. Muller, R. J. Birgeneau, R. Ramesh, Room-temperature skyrmion lattice in a layered magnet $(\text{Fe}_{0.5}\text{Co}_{0.5})_5\text{GeTe}_2$, *Adv. Sci.* **2022**, *8*, 12 eabm7103.

[33] A. F. May, D. Ovchinnikov, Q. Zheng, R. Hermann, S. Calder, B. Huang, Z. Fei, Y. Liu, X. Xu, M. A. McGuire, Ferromagnetism Near Room Temperature in the Cleavable van der Waals Crystal Fe_5GeTe_2 , *ACS Nano*. **2019**, *13*, 4 4436.

[34] J. M. J. Lopes, D. Czubak, E. Zallo, A. I. Figueroa, C. Guillemard, M. Valvidares, J. Rubio-Zuazo, J. López-Sánchez, S. O. Valenzuela, M. Hanke, M. Ramsteiner, Large-area van der Waals epitaxy and magnetic characterization of Fe_3GeTe_2 films on graphene, *2D Mater.* **2021**, *8*, 4 041001.

[35] G. Zhang, F. Guo, H. Wu, X. Wen, L. Yang, W. Jin, W. Zhang, H. Chang, Above-room-temperature strong intrinsic ferromagnetism in 2D van der Waals Fe_3GaTe_2 with large perpendicular magnetic anisotropy, *Nat. Commun.* **2022**, *13*, 1 5067.

[36] T. Shinwari, K. I. A. Khan, H. Lv, A. A. Kassa, F. Munnik, S. Josephy, A. Trampert, V. Ukleev, C. Luo, F. Radu, J. Herfort, M. Hanke, J. M. J. Lopes, Above-Room-Temperature Ferromagnetism in Large-Scale Epitaxial Fe_3GaTe_2 /Graphene van der Waals Heterostructures, *ACS Nano*. **2025**, *19*, 43 37561–37571.

[37] B. Dieny, M. Chshiev, Perpendicular magnetic anisotropy at transition metal/oxide interfaces and applications, *Rev. Mod. Phys.* **2017**, *89*, 2 025008.

[38] B. Dieny, I. L. Prejbeanu, K. Garello, P. Gambardella, P. Freitas, R. Lehndorff, W. Raberg, U. Ebels, S. O. Demokritov, J. Akerman, A. Deac, P. Pirro, C. Adelmann, A. Anane, A. V. Chumak, A. Hirohata, S. Mangin, S. O. Valenzuela, M. C. Onbaşlı, M. d’Aquino, G. Prenat, G. Finocchio, L. Lopez-Diaz, R. Chantrell, O. Chubykalo-Fesenko, P. Bortolotti, Opportunities and challenges for spintronics in the microelectronics industry, *Nat. Electron.* **2020**, *3*, 8 446.

[39] S. Ikeda, K. Miura, H. Yamamoto, K. Mizunuma, H. D. Gan, M. Endo, S. Kanai, J. Hayakawa, F. Matsukura, H. Ohno, A perpendicular-anisotropy CoFeB–MgO magnetic tunnel junction, *Nat. Mater.* **2010**, *9*, 9 721.

[40] S. Ikeda, H. Sato, M. Yamanouchi, H. Gan, K. Miura, K. Mizunuma, S. Kanai, S. Fukami, F. Matsukura, N. Kasai, H. Ohno, Recent progress of perpendicular anisotropy magnetic tunnel junctions for nonvolatile vlsi, *SPIN* **2012**, *02*, 03 1240003.

[41] W. Miao, W. Zhen, C. Tan, J. Wang, Y. Nie, H. Wang, L. Wang, Q. Niu, M. Tian, Nonreciprocal Antisymmetric Magnetoresistance and Unconventional Hall Effect in a Two-Dimensional Ferromagnet, *ACS Nano*. **2023**, *17*, 24 25449.

[42] Y. Deng, Z. Xiang, B. Lei, K. Zhu, H. Mu, W. Zhuo, X. Hua, M. Wang, Z. Wang, G. Wang, M. Tian, X. Chen, Layer-Number-Dependent Magnetism and Anomalous Hall Effect in van der Waals Ferromagnet Fe_5GeTe_2 , *Nano Lett.* **2022**, *22*, 24 9839.

[43] H. Zhang, R. Chen, K. Zhai, X. Chen, L. Caretta, X. Huang, R. V. Chopdekar, J. Cao, J. Sun, J. Yao, R. Birgeneau, R. Ramesh, Itinerant ferromagnetism in van der Waals $\text{Fe}_{5-x}\text{GeTe}_2$ crystals above room temperature, *Phys. Rev. B* **2020**, *102*, 6 064417.

[44] S. J. Kim, D. Choi, K.-W. Kim, K.-Y. Lee, D.-H. Kim, S. Hong, J. Suh, C. Lee, S. K. Kim, T.-E. Park, H. C. Koo, Interface Engineering of Magnetic Anisotropy in van der Waals Ferromagnet-based Heterostructures, *ACS Nano*. **2021**, *15*, 10 16395.

[45] I. Shin, W. J. Cho, E.-S. An, S. Park, H.-W. Jeong, S. Jang, W. J. Baek, S. Y. Park, D.-H. Yang, J. H. Seo, G.-Y. Kim, M. N. Ali, S.-Y. Choi, H.-W. Lee, J. S. Kim, S. D. Kim, G.-H. Lee, Spin–Orbit Torque Switching in an All–Van der Waals Heterostructure, *Adv. Mater.* **2022**, *34*, 8 2101730.

[46] W. Dong, Z. Dai, L. Liu, Z. Zhang, Toward Clean 2D Materials and Devices: Recent Progress in Transfer and Cleaning Methods, *Adv. Mater.* **2024**, *36*, 22 2303014.

[47] H. Zhu, N. Nayir, T. H. Choudhury, A. Bansal, B. Huet, K. Zhang, A. A. Puretzky, S. Bachu, K. York, T. V. Mc Knight, N. Trainor, A. Oberoi, K. Wang, S. Das, R. A. Makin, S. M. Durbin, S. Huang, N. Alem, V. H. Crespi, A. C. T. van Duin, J. M. Redwing, Step engineering for nucleation and domain orientation control in WSe₂ epitaxy on c-plane sapphire, *Nat. Nanotechnol.* **2023**, *18*, 11 1295.

[48] J. Li, X. Yang, Z. Zhang, W. Yang, X. Duan, X. Duan, Towards the scalable synthesis of two-dimensional heterostructures and superlattices beyond exfoliation and restacking, *Nat. Mater.* **2024**, *23*, 10 1326.

[49] C. Liu, T. Liu, Z. Zhang, Z. Sun, G. Zhang, E. Wang, K. Liu, Understanding epitaxial growth of two-dimensional materials and their homostructures, *Nat. Nanotechnol.* **2024**, *19*, 7 907.

[50] Q. Guillet, L. Vojáček, D. Dosenovic, F. Ibrahim, H. Boukari, J. Li, F. Choueikani, P. Ohresser, A. Ouerghi, F. Mesple, V. Renard, J.-F. m. c. Jacquot, D. Jalabert, H. Okuno, M. Chshiev, C. Vergnaud, F. Bonell, A. Marty, M. Jamet, Epitaxial van der waals heterostructures of Cr₂Te₃ on two-dimensional materials, *Phys. Rev. Mater.* **2023**, *7* 054005.

[51] A. F. May, C. A. Bridges, M. A. McGuire, Physical properties and thermal stability of Fe_{5-x}GeTe₂ single crystals, *Phys. Rev. Mater.* **2019**, *3*, 10 104401.

[52] S. Ershadrad, S. Ghosh, D. Wang, Y. Kvashnin, B. Sanyal, Unusual Magnetic Features in Two-Dimensional Fe₅GeTe₂ Induced by Structural Reconstructions, *J. Phys. Chem. Lett.* **2022**, *13*, 22 4877.

[53] T. Schumann, M. Dubslaff, M. H. Oliveira, M. Hanke, J. M. J. Lopes, H. Riechert, Effect of buffer layer coupling on the lattice parameter of epitaxial graphene on SiC(0001), *Phys. Rev. B* **2014**, *90* 041403.

[54] M. Nakano, Y. Wang, Y. Kashiwabara, H. Matsuoka, Y. Iwasa, Layer-by-Layer Epitaxial Growth of Scalable WSe₂ on Sapphire by Molecular Beam Epitaxy, *Nano Lett.* **2017**, *17*, 9 5595.

[55] M. Ribeiro, G. Gentile, A. Marty, D. Dosenovic, H. Okuno, C. Vergnaud, J.-F. Jacquot, D. Jalabert, D. Longo, P. Ohresser, A. Hallal, M. Chshiev, O. Boulle, F. Bonell, M. Jamet, Large-scale epitaxy of two-dimensional van der Waals room-temperature ferromagnet Fe₅GeTe₂, *npj 2D Mater. Appl.* **2022**, *6*, 1 10.

[56] W. Mortelmans, S. El Kazzi, A. Nalin Mehta, D. Vanhaeren, T. Conard, J. Meerschaut, T. Nuytten, S. De Gendt, M. Heyns, C. Merckling, Peculiar alignment and strain of 2D WSe₂ grown by van der Waals epitaxy on reconstructed sapphire surfaces, *Nanotechnology* **2019**, *30*, 46 465601.

[57] D. Voß, P. Krüger, A. Mazur, J. Pollmann, Atomic and electronic structure of WSe₂ from ab initio theory: Bulk crystal and thin film systems, *Phys. Rev. B* **1999**, *60*, 20 14311.

[58] D. Yang, X. Fan, F. Zhang, Y. Hu, Z. Luo, Electronic and Magnetic Properties of Defected Monolayer WSe₂ with Vacancies, *Nanoscale Res. Lett.* **2019**, *14*, 1 192.

[59] T. Schumann, M. Dubslaff, M. H. Oliveira, M. Hanke, F. Fromm, T. Seyller, L. Nemec, V. Blum, M. Scheffler, J. M. J. Lopes, H. Riechert, Structural investigation of nanocrystalline graphene grown on (6 $\sqrt{3}$ × 6 $\sqrt{3}$)R30°-reconstructed SiC surfaces by molecular beam epitaxy, *New J. Phys.* **2013**, *15*, 12 123034.

[60] J. E. Boschker, L. A. Galves, T. Flissikowski, J. M. J. Lopes, H. Riechert, R. Calarco, Coincident-site lattice matching during van der Waals epitaxy, *Sci. Rep.* **2015**, *5*, 1 18079.

[61] A. F. May, S. Calder, C. Cantoni, H. Cao, M. A. McGuire, Magnetic structure and phase stability of the van der Waals bonded ferromagnet $\text{Fe}_{3-x}\text{GeTe}_2$, *Phys. Rev. B* **2016**, *93*, 1 014411.

[62] W. Zhou, A. J. Bishop, X. S. Zhang, K. Robinson, I. Lyalin, Z. Li, R. Bailey-Crandell, T. M. J. Cham, S. Cheng, Y. K. Luo, D. C. Ralph, D. A. Muller, R. K. Kawakami, Tuning the Curie temperature of a two-dimensional magnet/topological insulator heterostructure to above room temperature by epitaxial growth, *Phys. Rev. Mater.* **2023**, *7*, 10 104004.

[63] D. C. Jiles, D. L. Atherton, Theory of ferromagnetic hysteresis (invited), *J. Appl. Phys.* **1984**, *55*, 6 2115.

[64] N. Nagaosa, J. Sinova, S. Onoda, A. H. MacDonald, N. P. Ong, Anomalous hall effect, *Rev. Mod. Phys.* **2010**, *82* 1539.

[65] J. Liang, S. Liang, T. Xie, A. F. May, T. Ersevim, Q. Wang, H. Ahn, C. Lee, X. Zhang, J.-P. Wang, M. A. McGuire, M. Ouyang, C. Gong, Facile integration of giant exchange bias in Fe_5GeTe_2 /oxide heterostructures by atomic layer deposition, *Phys. Rev. Mater.* **2023**, *7*, 1 014008.

[66] J. Nogués, I. K. Schuller, Exchange bias, *J. Magn. Magn. Mater.* **1999**, *192*, 2 203.

[67] M. Kiwi, Exchange bias theory, *J. Magn. Magn. Mater.* **2001**, *234*, 3 584.

[68] K. O'Grady, L. E. Fernandez-Outon, G. Vallejo-Fernandez, A new paradigm for exchange bias in polycrystalline thin films, *J. Magn. Magn. Mater.* **2010**, *322*, 8 883.

[69] H. Lv, D. C. Leitao, K. Pruegl, W. Raberg, P. P. Freitas, S. Cardoso, Impact of blocking temperature distribution on the thermal behavior of MnIr and MnPt magnetoresistive stacks, *J. Magn. Magn. Mater.* **2019**, *477* 68.

[70] A. Puthirath Balan, A. Kumar, T. Scholz, Z. Lin, A. Shahee, S. Fu, T. Denneulin, J. Vas, A. Kovács, R. E. Dunin-Borkowski, H. I. Wang, J. Yang, B. V. Lotsch, U. Nowak, M. Kläui, Harnessing Van der Waals CrPS_4 and Surface Oxides for Nonmonotonic Preset Field Induced Exchange Bias in Fe_3GeTe_2 , *ACS Nano.* **2024**, *18*, 11 8383.

[71] J. Shao, X. Yin, C. Bao, S. Lu, X. Ma, S. Guo, L. Wang, X. Zhang, Z. Li, L. Li, Y. Zhao, T. Chen, Near-Room-Temperature Field-Controllable Exchange Bias in 2D van der Waals Ferromagnet Fe_3GaTe_2 , **2024**, URL <http://arxiv.org/abs/2406.02260>.

[72] S. Hu, X. Cui, Z. Yue, P. Wang, L. Guo, K. Ohnishi, X. Wang, T. Kimura, The positive exchange bias property with hopping switching behavior in van der Waals magnet FeGeTe , *2D Mater.* **2022**, *9*, 1 015037.

[73] M.-H. Phan, V. Kalappattil, V. O. Jimenez, Y. Thi Hai Pham, N. W. Y. A. Y. Mudiyanselage, D. Detellem, C.-M. Hung, A. Chanda, T. Eggers, Exchange bias and interface-related effects in two-dimensional van der Waals magnetic heterostructures: Open questions and perspectives, *J. Alloys Compd.* **2023**, *937* 168375.

[74] Y. Guo, Y. Zhao, S. Zhou, J. Zhao, Oxidation behavior of layered Fe_nGeTe_2 ($n = 3, 4, 5$) and $\text{Cr}_2\text{Ge}_2\text{Te}_6$ governed by interlayer coupling, *Nanoscale* **2022**, *14*, 31 11452.

[75] S. J. Yun, K.-J. Lee, S. H. Lim, Critical switching current density induced by spin Hall effect in magnetic structures with first- and second-order perpendicular magnetic anisotropy, *Sci. Rep.* **2017**, *7*, 1 15314.

[76] A. A. Timopheev, R. Sousa, M. Chshiev, H. T. Nguyen, B. Dieny, Second order anisotropy contribution in perpendicular magnetic tunnel junctions, *Sci. Rep.* **2016**, *6*, 1 26877.

[77] A. Bera, N. Jana, A. Agarwal, S. Mukhopadhyay, Anisotropic magnetization dynamics in Fe_5GeTe_2 at room temperature, *Phys. Rev. B* **2024**, *110*, 22 224401.

[78] B. Zhao, R. Ngaloy, S. Ghosh, S. Ershadrad, R. Gupta, K. Ali, A. M. Hoque, B. Karpiak, D. Khokhriakov, C. Polley, B. Thiagarajan, A. Kalaboukhov, P. Svedlindh, B. Sanyal, S. P. Dash, Room Temperature Spin-Valve with van der Waals Ferromagnet Fe_5GeTe_2 /Graphene Heterostructure, *Adv. Mater.* **2023**, *35*, 16 2209113.

[79] B. Zhao, L. Pandey, K. Ali, E. Wang, C. M. Polley, B. Thiagarajan, P. Makk, M. H. D. Guimarães, S. P. Dash, Field-Free Spin–Orbit Torque Switching of Canted van der Waals Magnets, *ACS Nano* **2025**, *19*, 14 13817.

[80] H. Zhang, X. Chen, T. Wang, X. Huang, X. Chen, Y.-T. Shao, F. Meng, P. Meisenheimer, A. N'Diaye, C. Klewe, P. Shafer, H. Pan, Y. Jia, M. F. Crommie, L. W. Martin, J. Yao, Z. Qiu, D. A. Muller, R. J. Birgeneau, R. Ramesh, Room-Temperature, Current-Induced Magnetization Self-Switching in A Van Der Waals Ferromagnet, *Adv. Mater.* **2024**, *36*, 9 2308555.

[81] Y. You, Y. Gong, H. Li, Z. Li, M. Zhu, J. Tang, E. Liu, Y. Yao, G. Xu, F. Xu, W. Wang, Angular dependence of the topological Hall effect in the uniaxial van der Waals ferromagnet Fe_3GeTe_2 , *Phys. Rev. B* **2019**, *100*, 13 134441.

[82] P. Ritzinger, K. Výborný, Anisotropic magnetoresistance: materials, models and applications, *R. Soc. Open Sci.* **2023**, *10*, 10 230564.

[83] H. Lv, X. C. Huang, K. H. L. Zhang, O. Bierwagen, M. Ramsteiner, Underlying Mechanisms and Tunability of the Anomalous Hall Effect in NiCo_2O_4 Films with Robust Perpendicular Magnetic Anisotropy, *Adv. Sci.* **2023**, *10*, 28 2302956.

[84] H. Lv, J. Herfort, M. Hanke, C. Chen, J. M. Redwing, A. Trampert, R. Engel-Herbert, M. Ramsteiner, J. M. J. Lopes, All-Epitaxial $\text{Fe}_{5-x}\text{GeTe}_2$ /Graphene and $\text{Fe}_{5-x}\text{GeTe}_2/\text{WSe}_2$ van der Waals Heterostructures With Above Room Temperature Ferromagnetism, *IEEE Trans. Magn.* **2024**, *60*, 9 1.

[85] P. K. Sivakumar, B. Göbel, E. Lesne, A. Markou, J. Gidugu, J. M. Taylor, H. Deniz, J. Jena, C. Felser, I. Mertig, S. S. P. Parkin, Topological Hall Signatures of Two Chiral Spin Textures Hosted in a Single Tetragonal Inverse Heusler Thin Film, *ACS Nano* **2020**, *14*, 10 13463.

[86] Y. Wu, S. Zhang, J. Zhang, W. Wang, Y. L. Zhu, J. Hu, G. Yin, K. Wong, C. Fang, C. Wan, X. Han, Q. Shao, T. Taniguchi, K. Watanabe, J. Zang, Z. Mao, X. Zhang, K. L. Wang, Néel-type skyrmion in $\text{WTe}_2/\text{Fe}_3\text{GeTe}_2$ van der Waals heterostructure, *Nat. Commun.* **2020**, *11*, 1 3860.

[87] Y. Zhou, S. Li, X. Liang, Y. Zhou, Topological Spin Textures: Basic Physics and Devices, *Adv. Mater.* **2025**, *37*, 2 2312935.

[88] F. Zheng, N. S. Kiselev, F. N. Rybakov, L. Yang, W. Shi, S. Blügel, R. E. Dunin-Borkowski, Hopfion rings in a cubic chiral magnet, *Nature* **2023**, *623*, 7988 718.

[89] K. Litzius, I. Lemesh, B. Krüger, P. Bassirian, L. Caretta, K. Richter, F. Büttner, K. Sato, O. A. Tretiakov, J. Förster, R. M. Reeve, M. Weigand, I. Bykova, H. Stoll, G. Schütz, G. S. D. Beach, M. Kläui, Skyrmion Hall effect revealed by direct time-resolved X-ray microscopy, *Nat. Phys.* **2017**, *13*, 2 170.

[90] A. Fert, V. Cros, J. Sampaio, Skyrmions on the track, *Nat. Nanotechnol.* **2013**, *8*, 3 152.

[91] S. Parkin, S.-H. Yang, Memory on the racetrack, *Nat. Nanotechnol.* **2015**, *10*, 3 195.

[92] T. da Câmara Santa Clara Gomes, Y. Sassi, D. Sanz-Hernández, S. Krishnia, S. Collin, M.-B. Martin, P. Seneor, V. Cros, J. Grollier, N. Reyren, Neuromorphic weighted sums with magnetic skyrmions, *Nat. Electron.* **2025**, *8*, 3 204.

[93] J. M. J. Lopes, H. Lv, J. Herfort, M. Hanke, C. Chen, J. M. Redwing, A. Trampert, R. Engel-Herbert, M. Ramsteiner, In *INTERMAG Short papers*. **2024** 1–2, URL <https://ieeexplore.ieee.org/document/10577072/?arnumber=10577072>.

[94] M. Alghamdi, P. R. Jothi, W.-C. Liao, S. Coh, X. Lin, B. P. T. Fokwa, J. Shi, Layer-dependence study of two-dimensional ferromagnets: Fe_3GeTe_2 and $\text{Fe}_5\text{Ge}_2\text{Te}_2$, *Appl. Phys. Lett.* **2024**, *124*, 19 192404.

[95] V. W. Guo, B. Lu, X. Wu, G. Ju, B. Valcu, D. Weller, A survey of anisotropy measurement techniques and study of thickness effect on interfacial and volume anisotropies in Co/Pt multilayer media, *J. Appl. Phys.* **2006**, *99*, 8 08E918.

[96] K. Yakushiji, T. Saruya, H. Kubota, A. Fukushima, T. Nagahama, S. Yuasa, K. Ando, Ultrathin Co/Pt and Co/Pd superlattice films for MgO-based perpendicular magnetic tunnel junctions, *Appl. Phys. Lett.* **2010**, *97*, 23 232508.

[97] D. C. Worledge, G. Hu, D. W. Abraham, J. Z. Sun, P. L. Trouilloud, J. Nowak, S. Brown, M. C. Gaidis, E. J. O'Sullivan, R. P. Robertazzi, Spin torque switching of perpendicular Ta|CoFeB|MgO-based magnetic tunnel junctions, *Appl. Phys. Lett.* **2011**, *98*, 2 022501.

[98] G. Ma, R. Du, F. Lian, S. Bao, Z. Guo, X. Cai, J. Xiao, Y. Han, D. Zhang, S. Jiang, J. Huang, X. Wu, A. S. Mayorov, J. Wen, L. Wang, G. Yu, Tailoring coercive fields and the Curie temperature via proximity coupling in $\text{WSe}_2/\text{Fe}_3\text{GeTe}_2$ van der Waals heterostructures, *2D Mater.* **2024**, *11*, 3 035020.